remote sensing

MDPI

Communication

Influence of the Coriolis Force on Spreading of River Plumes

Alexander Osadchiev [1,2,*], Ivan Alfimenkov [3] and Vladimir Rogozhin [1,4]

[1] Shirshov Institute of Oceanology, Russian Academy of Sciences, Nahimovskiy Prospect 36, 117997 Moscow, Russia; rogozhin.vs@ocean.ru
[2] Moscow Institute of Physics and Technology, Institusky Lane 9, 141701 Dolgoprudny, Russia
[3] Hydrology and Oceanology Department, Russian State Hydrometeorological University, Malookhtinskiy Prospekt 98, 195196 St. Petersburg, Russia
[4] Marine Research Center at Lomonosov Moscow State University, Leninskie Gory 1, 119992 Moscow, Russia
* Correspondence: osadchiev@ocean.ru

Abstract: Wind is the main external force that governs the spreading of river plumes in the sea. Many previous studies demonstrated that the spreading direction of river plumes (especially small plumes) generally coincides with wind direction. At the same time, the majority of river plumes are strongly affected by the Coriolis force, which is also among the baseline knowledge about the plumes. In this study, we focus on the deflection of plumes from wind direction induced by the Coriolis force, which received little attention before. For this purpose, we analyzed an extensive set of Landsat 8 and Sentinel-2 satellite images of multiple small- and medium-sized river plumes at different parts of the World Ocean and synchronous wind reanalysis data. We demonstrated that the deflection angle is stable for individual river plumes for different wind directions, albeit with certain limitations related to wind speed and coastal morphology. Moreover, the deflection angle is similar for river plumes located at similar latitudes and varies from ~0° near the Equator to 15–25° in temperate zones and ~30° in polar zones. Finally, we derived a direct relation between latitude and the deflection angle. The obtained results contribute to our understanding of universal features of river plume dynamics, which is important for monitoring and forecasting of delivery and fate of fluvial water and river-borne matter in different coastal regions of the World Ocean.

Keywords: river plume; Coriolis force; wind forcing; coastal circulation; Ekman transport

Citation: Osadchiev, A.; Alfimenkov, I.; Rogozhin, V. Influence of the Coriolis Force on Spreading of River Plumes. *Remote Sens.* **2023**, *15*, 3397. https://doi.org/10.3390/rs15133397

Academic Editors: Angelica Tarpanelli, José Darrozes and Alfonso Vitti

Received: 16 May 2023
Revised: 16 June 2023
Accepted: 3 July 2023
Published: 4 July 2023

1. Introduction

River discharge is the main source of haline stratification of the surface layer at many coastal and shelf regions in the World Ocean [1,2]. River runoffs form river plumes, which play the role of narrow transition zones for land–ocean fluxes of fluvial water. River plumes generally occupy the wide yet shallow sea surface layer bound by a sharp density gradient. The area of a river plume is 3–5 orders of magnitude greater than its depth; therefore, even small rivers with discharge rates ~1–10 m^3/s form river plumes with horizontal spatial extents ~10–100 m. The areas of river plumes formed by the largest world rivers are ~100–1000 km^2. Despite the relatively small volume of total freshwater runoff to the World Ocean, river plumes occupy up to 1/5 of shelf areas of the World Ocean [2] and substantially influence global fluxes of buoyancy, heat, terrigenous sediments, nutrients, and anthropogenic pollutants, which are discharged into the coastal sea with continental runoff [3–6]. River plumes generally constantly receive a freshwater discharge from their sources in river mouths and, at the same time, are constantly mixing with the ambient sea at their bottom and lateral boundaries [7–10]. Moreover, river plumes have energetic internal dynamics. Their sizes, shapes, and positions change in response to the variability of river discharge rate, wind, tide, and coastal circulation. As a result, river plumes are complex structures that are constantly changing to keep the dynamical and source-sink balance under varying external forcing conditions.

Wind forcing is the main driver of the short-term variability of river plumes, which was demonstrated in numerous previous studies [11–15]. This feature is caused by the coincidence of river plumes with the surface Ekman layer due to large density gradients at vertical plume-sea interfaces. The influence of the Coriolis force on river plumes (i.e., deflection to the right/left in the Northern/Southern hemispheres caused by Earth's rotation) could be quantified using the Rossby number Ro = U/L·f, where U is the typical velocity of a river plume, L is the typical horizontal scale of a river plume, f is the Coriolis frequency [16]. Once Ro < 1, a river plume is affected by the Coriolis force. The velocities in river plumes generally have an order of 0.1 m/s; as a result, Ro < 1 in the case of L·f > 0.1. This condition is met for the majority of latitudes (with $f > 10^{-5}$, i.e., except equatorial latitudes) in case of L > 10 km. The ratio between river discharge rate Q and river plume area S is stable and equal to 0.5×10^{-6} for a wide variety of river plumes with horizontal scales from ~100 m to ~100 km. Therefore, the Coriolis force is significant for plumes, which are formed by rivers with runoff > 50 m^3/s, except those in equatorial latitudes.

Under the first approximation, the motion of these river plumes could be described by the Ekman theory [17]. However, the motion equations for the Ekman layer are solved under several assumptions, which are not true for river plumes. In particular, the eddy viscosity does not remain constant within river plumes due to sharp vertical salinity gradients (especially at small plumes) and non-homogenous turbulence distribution. The presence of the salinity gradient dramatically reduces vertical eddy viscosity, which determines friction strength between two sea layers [18]. This effect hinders the formation of the Coriolis curl, i.e., wind energy transferred to the sea remains within the plume and limitedly penetrates below the plume-sea interface [19]. As a result, the surface currents in river plumes do not flow at a 45° angle to the wind, which is predicted by the Ekman theory [20]. Moreover, significant horizontal variability in vertical stratification within individual river plumes could result in different angles between surface currents and wind for near-field (affected by the inertia of inflowing river jet) and far-field (wind-driven) parts of a plume [21]. Nevertheless, this question received very little attention in previous studies despite its importance, from general numerical modeling of river plumes to understanding transport patterns of fluvial water in coastal seas.

In this study, we analyze optical satellite imagery (Sentinel-2 and Landsat 8) of river plumes located in different parts of the World Ocean. We determine the spreading directions of far-field parts of these plumes detected in satellite images (however, in many cases, they could not be determined) and compare them with synchronous wind data obtained from ERA5 reanalysis. Based on this data, we calculate the difference between these directions, which is regarded as the deflection angle. The main questions, which are addressed in this study, are the following: (1) is this deflection stable for individual river plumes under various wind forcing conditions, and (2) is this deflection stable for different river plumes at similar latitudes.

This paper is organized as follows. In Section 2, we provide information about the considered river plumes, as well as the satellite and wind reanalysis data used in the study. Section 3 described the relation between the plume's spreading direction on the one hand and wind-forcing conditions for river plumes located at different latitudes. The discussion about the importance of the obtained results for the assessment of the spreading of fluvial water and river-borne matter in the World Ocean is given in Section 4.

2. Data and Methods

In this study, we analyzed the spreading of thirty river plumes located in different regions of the World Ocean (Figure 1, Table 1). The latitudes of these plumes are spanned from 50°S in the south to 76°N in the north, including equatorial, tropical, subtropical, temperate, subpolar, and polar zones. At all zones, we selected plumes from both the Southern Hemisphere and the Northern Hemisphere, except subpolar and polar latitudes due to the absence of rivers at these zones in the Southern Hemisphere. The average discharge rates of these rivers vary from 50 to 2100 m^3/s; therefore, the considered plumes

are small- and medium-sized. As a result, these plumes have a relatively quick response to the variability of wind forcing [13,14].

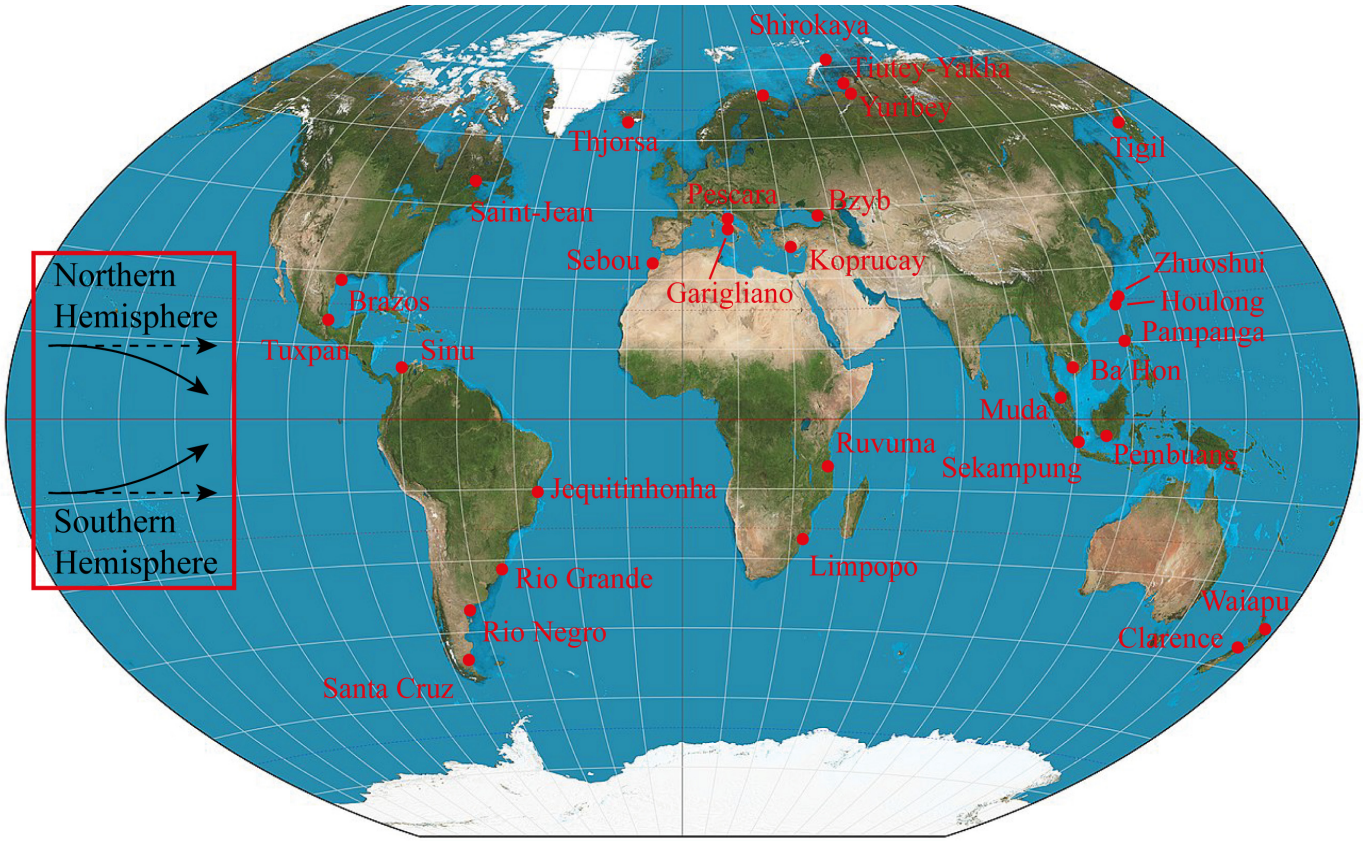

Figure 1. Locations of river plumes analyzed in this study. The inset in the red box demonstrates the effect of the Coriolis force in the Northern and Southern hemispheres, solid lines indicate intended paths, and the dashed lines indicate paths influenced by the Coriolis effect.

Satellite images of river plumes analyzed in this study consist of Sentinel-2 MSI and Landsat 8 OLI data collected in 2013–2022. Circulation streamlines at a far-field plume are parallel to the sharp and narrow outer frontal zone of a plume, which is often distinctly visible in satellite imagery [21]. Therefore, the spreading direction of a river plume in a cloud-free satellite image was determined according to the location of the sharp outer front at the far-field part of the plume. Wind forcing conditions were examined using ERA5 atmospheric reanalysis with a 0.25° spatial and hourly temporal resolution [22].

Table 1. Locations, watershed basin areas, and average discharge rates of rivers analyzed in this study.

River (Region)	Location of River Mouth	Watershed Basin Area, km^2	Average Discharge Rate, m^3/s
Shirokaya (Novaya Zemlya)	76.085°N, 67.181°E	- *	- *
Tiutey-Yakha (Yamal)	71.421°N, 67.580°E	3200	50
Yuribey (Yamal)	68.891°N, 68.852°E	9700	80
Thjorsa (Iceland)	63.773°N, 20.797°W	7500	390
Tigil (Kamchatka)	58.024°N, 158.2017°E	17,800	200
Saint-Jean (Labrador)	50.279°N, 64.334°W	5600	130
Bzyb (Abkhazia)	43.186°N, 40.281°E	1500	100
Pescara (Italy)	42.469°N, 14.231°E	3200	60
Garigliano (Italy)	41.222°N, 13.762°E	5000	120
Koprucay (Turkey)	36.828°N, 31.170°E	2400	100
Sebou (Morocco)	34.266°N, 6.687°W	14,600	140
Brazos (Texas)	28.876°N, 95.378°W	116,000	240
Houlong (Taiwan)	24.625°N, 120.742°E	540	50
Zhuoshui (Taiwan)	23.841°N, 120.239°E	3200	170
Tuxpan (Mexico)	20.972°N, 97.300°W	5900	2100
Pampanga (Luzon)	14.768°N, 120.656°E	9800	
Ba Hon (Vietnam)	10.243°N, 104.583°W	- **	- **
Sinu (Colombia)	9.444°N, 75.952°W	13,700	450
Muda (Malaysia)	5.567°N, 100.323°E	4300	110
Pembuang (Borneo)	3.434°S, 112.567°E	12,900	1200
Sekampung (Sumatra)	5.577°S, 105.814°E	5700	240
Ruvuma (Tanzania)	10.474°S, 40.437°E	155,500	475
Jequitinhonha (Brazil)	15.850°S, 38.857°W	78,500	410
Doce (Brazil)	19.656°S, 39.815°W	86,200	900
Limpopo (Mozambique)	25.221°S, 33.517°E	415,000	170
Rio Grande (Brazil)	32.199°S, 52.071°W	200,000	1200
Waiapu (New Zealand)	37.814°S, 178.386°E	1700	80
Rio Negro (Patagonia)	41.044°S, 62.782°W	95,000	860
Clarence (New Zealand)	42.174°S, 173.931°E	3300	50
Santa Cruz (Patagonia)	50.133°S, 68.343°W	29,700	800

* There are no data about the watershed basin area and average discharge rate because this river is fed by the melting glacier during the summer season. ** There are no data about the watershed basin area and average discharge rate because this is the irrigation channel of the Mekong River, i.e., part of the Mekong River basin with artificially controlled discharge.

Deflection angles analyzed in this study were calculated as differences between wind direction (obtained from atmospheric reanalysis) and plume spreading direction (obtained from satellite imagery) using the following methodology. First, the outer up-wind plume front was detected by satellite imagery using the Canny edge method described in detail in [10]. Second, the tangent vector was calculated for all pixels at the reconstructed plume front curve starting from the seashore. Once the direction of the tangent vector becomes stable (with variability < 10°) for pixels of the curve, this direction was regarded as the plume spreading direction. Finally, the sign-dependent difference between wind direction and plume spreading direction was calculated with positive/negative values for the deflection of plume spreading wind to the right/left from the wind direction. The accuracy of the presented method of calculation of deflection angles is estimated as 10° according to the accuracy of the ERA5 wind direction and the accuracy of calculation of the tangent vector.

3. Results

Joint analysis of satellite imagery and wind forcing conditions provide an opportunity to determine the spreading direction of a river plume and wind direction. First, we investigated whether the difference between these angles, i.e., the deflection angle, is stable for individual river plumes. For this purpose, we selected 10–30 cloud-free images of individual river plumes located at different latitudes (Figure 1 and Table 1) with distantly visible sharp plume borders. We considered only river plumes formed at areas with

relatively straight and ordinary shorelines without large bays, capes, seawalls, breakwaters, islands, etc., which affect the spreading of river plumes.

We revealed that in the case of moderate wind forcing (>2 m/s) with stable direction (changes < 45° during 12 h), the deflection angle varies in a narrow range of 10–15° for all considered river plumes. In particular, the deflection angle remains stable for different wind directions (as for the Thjorsa plume in Figure 2). This feature is not observed only for wind directions, which press the plume onshore and arrest it near the coast, i.e., resulting in the absence of plume spreading direction. Similarly, the deflection angle remains stable for different wind speeds (as for the Brazos plume in Figure 3) except for light winds (Figure 3a).

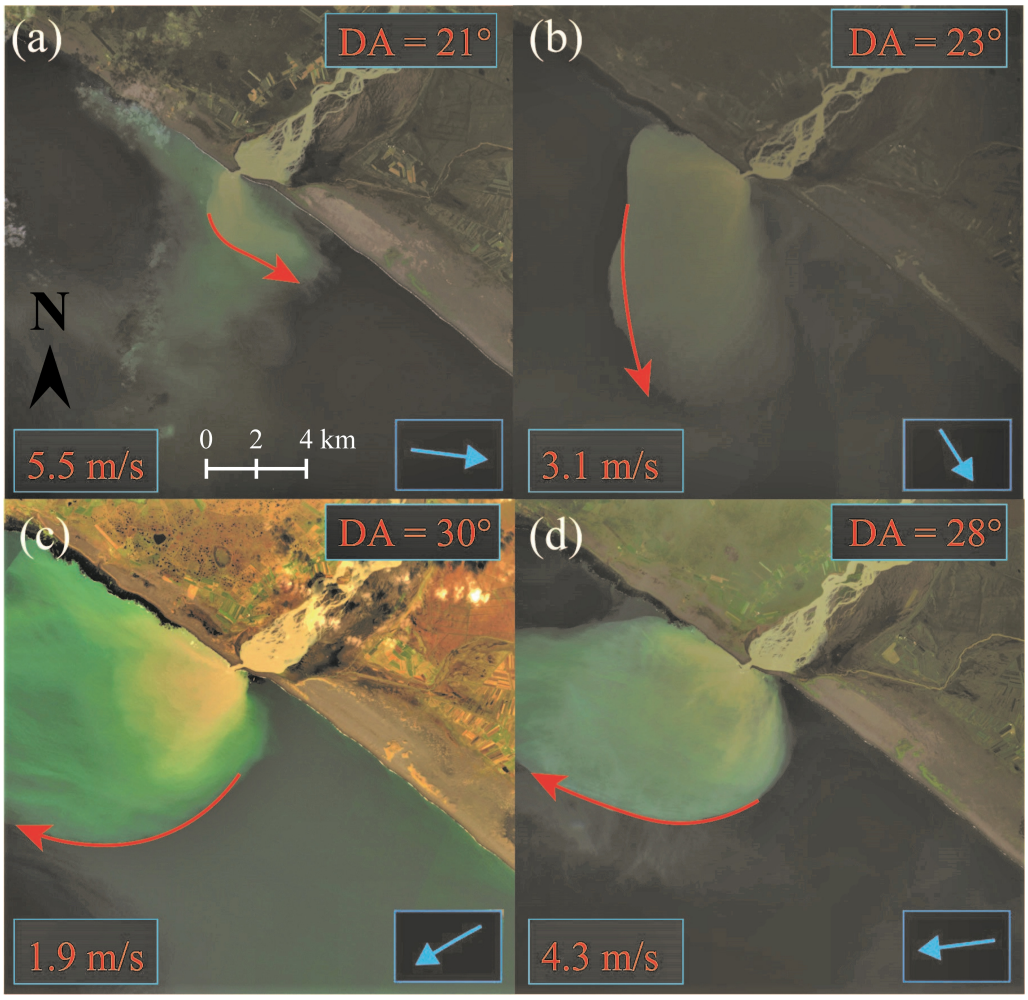

Figure 2. Sentinel-2 satellite images of the Thjorsa plume (63.773°N) under different wind direction conditions on (**a**) 28 July 2020, (**b**) 2 September 2019, (**c**) 30 September 2019, and (**d**) 22 August 2020. Red arrows illustrate the spreading directions of the Thjorsa plume, and blue arrows illustrate wind directions. Wind velocities and deflection angles (DA) are denoted at the related panels.

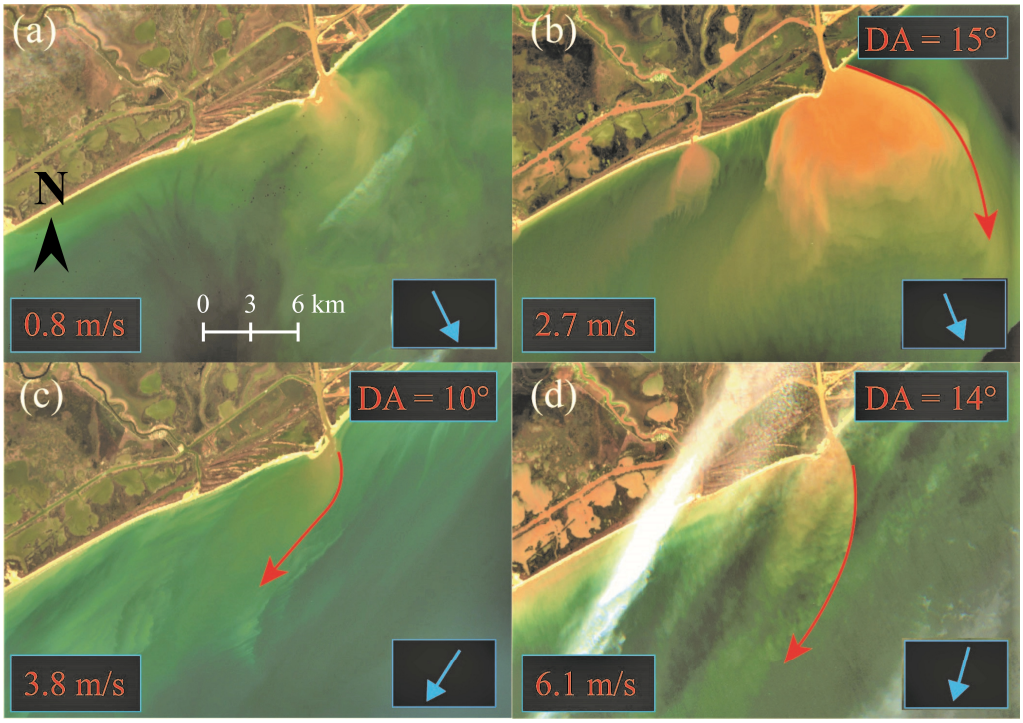

Figure 3. Sentinel-2 satellite images of the Brazos plume (28.877°N) under different wind speed conditions on (**a**) 10 February 2022, (**b**) 10 December 2018, (**c**) 27 December 2022, and (**d**) 10 February 2023. The red arrows illustrate the spreading directions of the Brazos Plume, and the blue arrows illustrate wind directions. The wind velocities and deflection angles (DA) are denoted at the related panels.

Based on the obtained results, we could state that under certain limitations, the deflection angle is stable for individual river plumes under various wind-forcing conditions. Furthermore, we compared magnitudes of deflection angles among river plumes located at similar latitudes. For this purpose, we selected sets of different plumes in equatorial (10°N–10°S), tropical (10–25°N and 10–25°S), subtropical (25–35°N and 25–35°S), temperate (35–50°N and 35–50°S), subpolar (50–65°N), and polar (65–80°N) latitudes. In all cases, deflection angles showed relatively small variability for plumes located in the same geographical zones. In particular, deflection angles varied in ranges of 0–10° for equatorial latitudes (Figure 4) and 15–25° for temperate latitudes (Figure 5). Moreover, the deflection angles steadily increased with an increase in latitudes from ~0° near the Equator to ~30° in the polar zones (Figure 6). Note that in Figures 4–6, the clockwise rotation from the wind direction to the plume spreading direction is regarded as a positive deflection angle (observed in the Northern Hemisphere), while the counterclockwise rotation is regarded as a negative deflection angle (observed in the Southern Hemisphere).

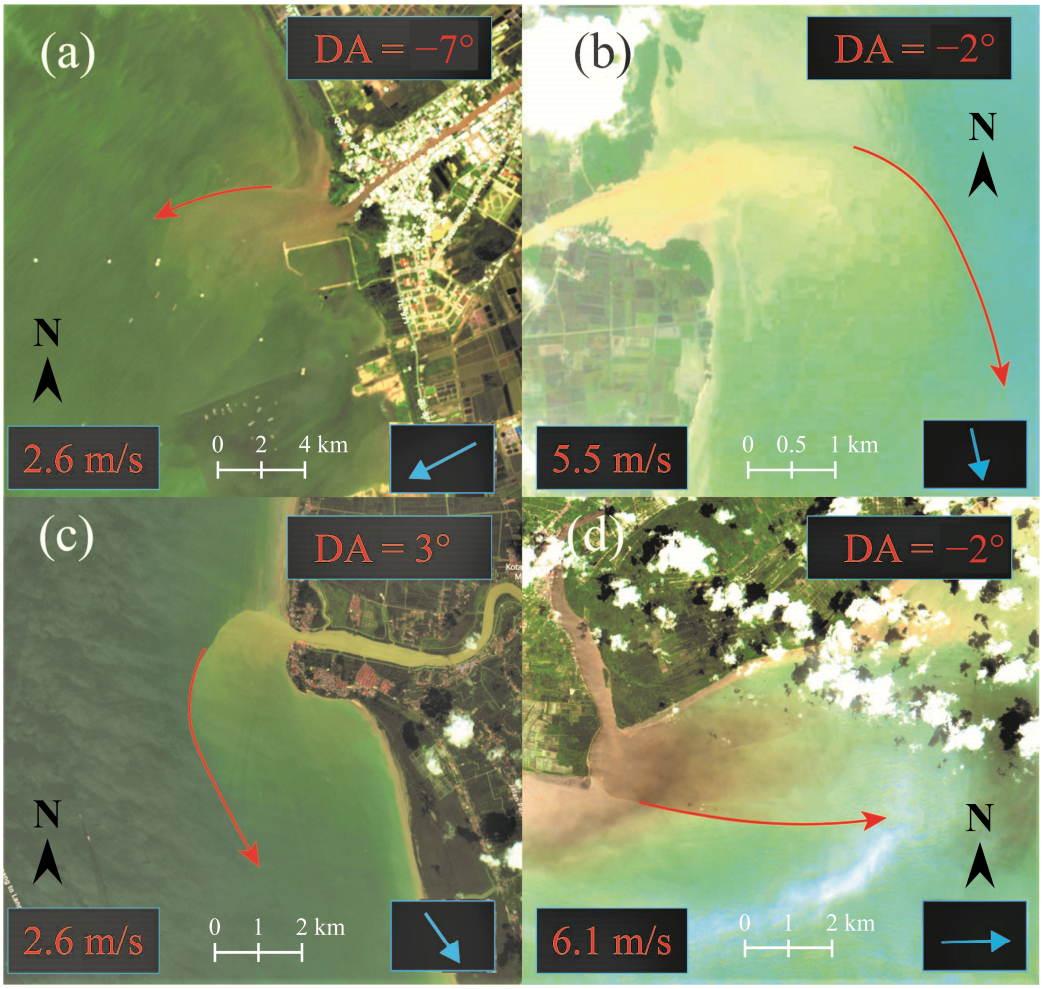

Figure 4. Sentinel-2 satellite images of river plumes located at similar equatorial latitudes: (**a**) Ba Hon plume (10.244°N) on 26 November 2021, (**b**) Sekampung plume (5.575°S) on 4 January 2023, (**c**) Muda plume (5.577°N) on 12 December 2020, and (**d**) Pembuang plume (3.434°S) on 17 February 2023. The red arrows illustrate the spreading directions of the river plume, and the blue arrows illustrate the wind directions. The wind velocities and the deflection angles (DA) are denoted at the related panels.

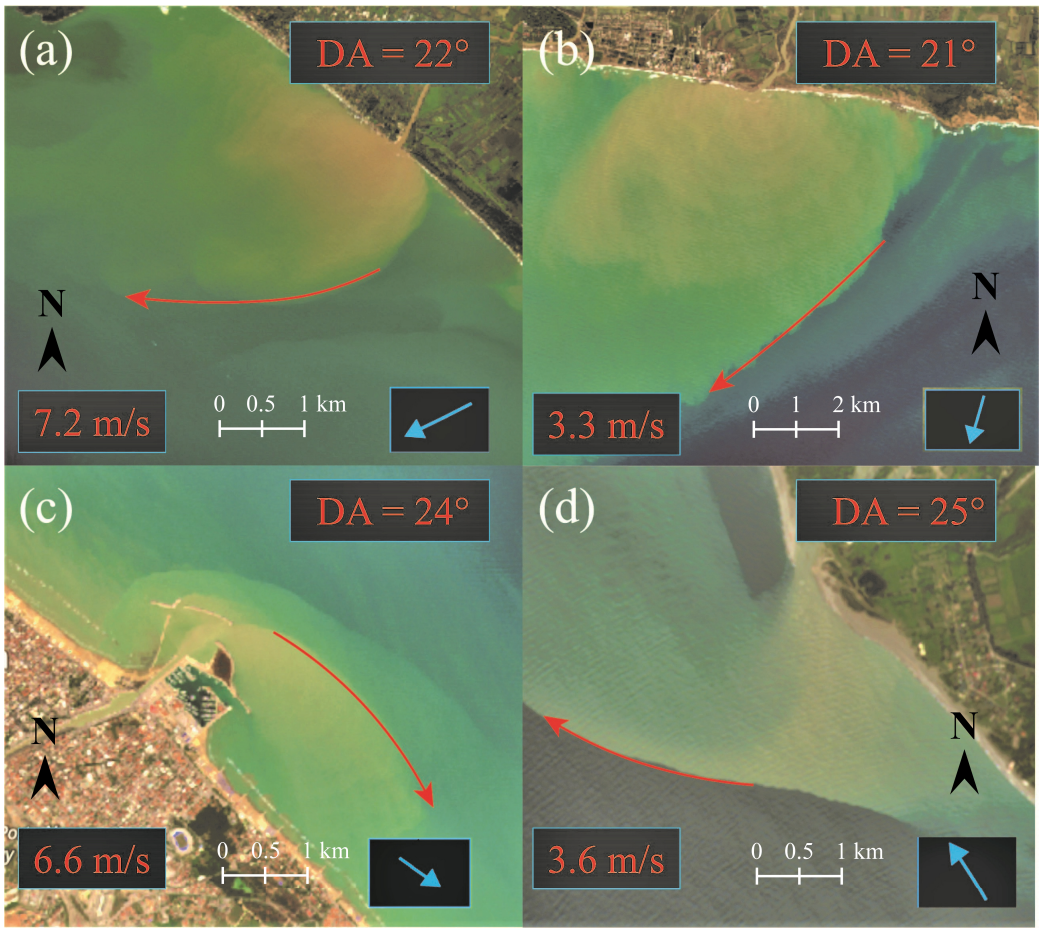

Figure 5. Sentinel-2 satellite images of river plumes located at similar temperate latitudes: (**a**) Garigliano plume (41.222°N) on 11 December 2022, (**b**) Koprucay plume (36.828°N) on 1 February 2019, (**c**) Pescara plume (42.469°N) on 11 June 2022, and (**d**) Bzyb plume (43.186°N) on 16 April 2018. The red arrows illustrate the spreading directions of the river plume, and the blue arrows illustrate the wind directions. The wind velocities and deflection angles (DA) are denoted at the related panels.

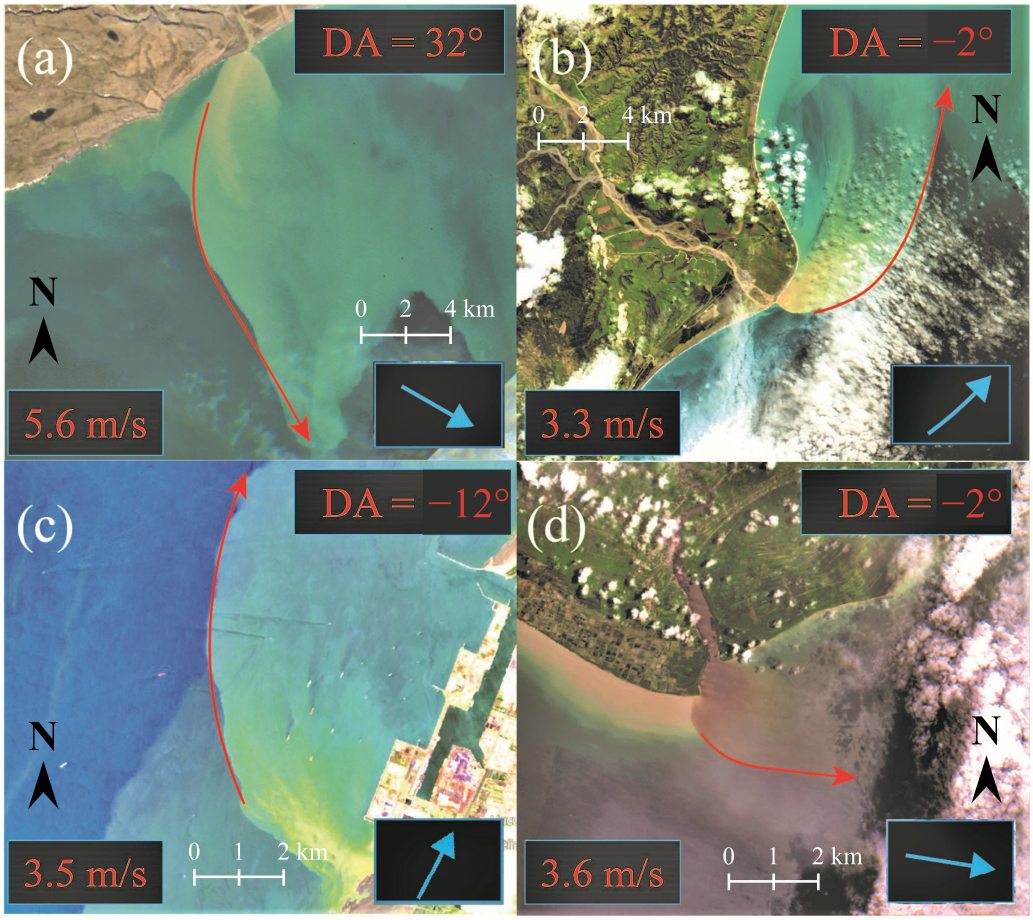

Figure 6. Sentinel-2 satellite images of river plumes located at different latitudes: (**a**) Shirokaya plume (76.085°N) on 10 August 2022, (**b**) Clarence plume (42.172°S) on 18 October 2019, (**c**) Houlong plume (24.201°N) on 3 August 2022, and (**d**) Pembuang plume (3.434°N) on 19 March 2021. The red arrows illustrate the spreading directions of the plumes, and the blue arrows illustrate wind directions. The latitudes of river estuaries, wind velocities, and deflection angles (DA) are denoted at the related panels.

Finally, we obtained the relation between wind direction and plume spreading direction, which depend on the latitude. The reconstructed deflection angles for river plumes located at different geographical zones provided the linear dependence A = 0.45·L between plume deflection angle A and latitude L (Figure 7). This relation is consistent with previous analytical studies of the wind-induced Ekman layer [23,24]. The coefficient of determination R^2 for this relation is equal to 0.91. The root mean square error of this relation is equal to 5.3°, which is smaller than the accuracy of deflection angle calculation (10°), as described in Section 2.

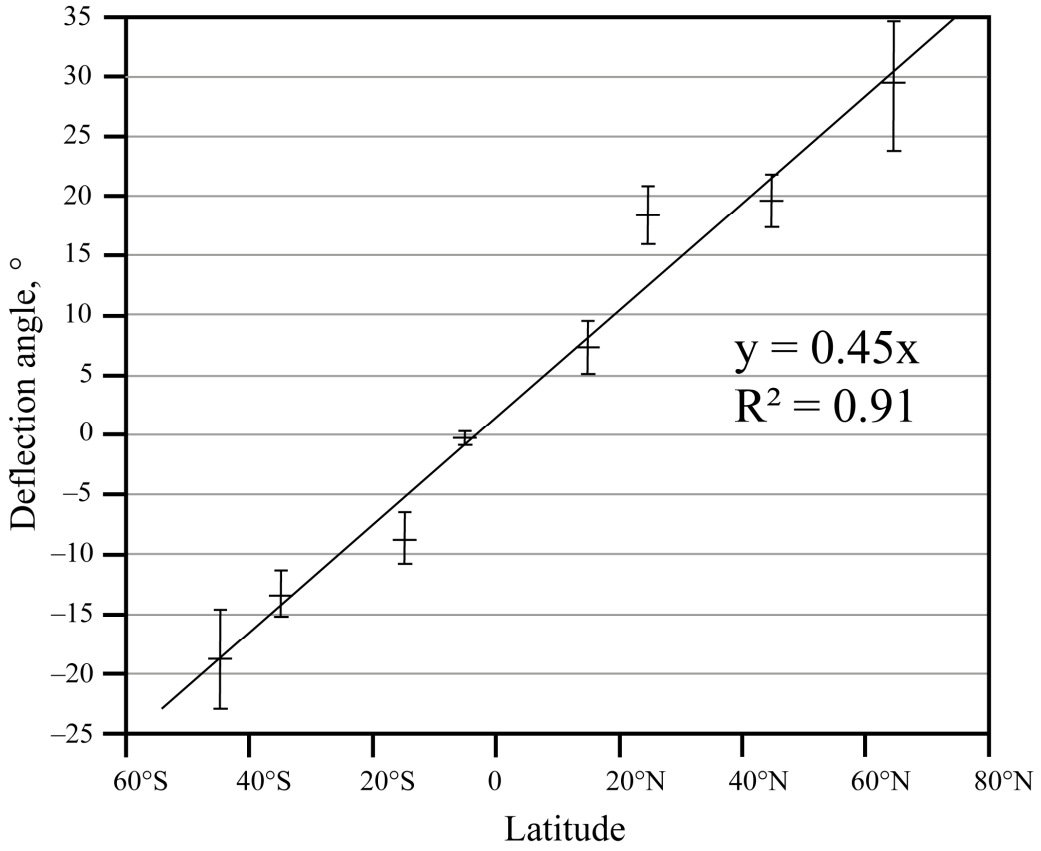

Figure 7. The relation between latitude and deflection angle for small- and medium-sized river plumes. The black line indicates the linear trend, and the whiskers indicate 95% confidence intervals.

4. Discussion and Conclusions

Wind forcing is among the main drivers of the spreading of river plumes. In this study, we investigated wind-induced spreading of small- and medium-sized plumes, in particular, the angle between wind direction and plume spreading direction. Using satellite imagery, we analyzed the variability of this deflection angle for eight river plumes located at different parts of the World Ocean in all geographical zones from polar latitudes to the Equator. First, we revealed that the deflection angle is stable for individual river plumes under various wind-forcing conditions. Second, we demonstrated that the deflection angle is stable for different river plumes at similar latitudes. Finally, we described the direct linear relation between the latitude and deflection angle for small- and medium-sized river plumes. The accuracy of this relation is estimated as 10°.

The obtained results are important for monitoring and numerical modeling of river plumes in many coastal regions of the World Ocean, especially those with a lack of in situ measurements. In addition, the obtained relation is important for the assessment of global land-ocean fluxes of fluvial water and river-borne matter, which significant share is provided by small- and medium-sized river plumes [25,26]. Nevertheless, we do not recommend a straightforward application of the obtained dependence between latitude and deflection angle due to the following reasons.

First, the stable spreading direction of a river plume with a distinct deflection angle is formed only under stable and durable wind forcing due to the quick response of river plumes to the variability of wind forcing conditions [14,27,28]. Second, winds of certain directions (which generally depend on latitude) press river plumes towards the shore and no spreading direction of river plume is formed. As a result, no deflection angle could be determined [19]. Third, features of the shoreline, both natural (e.g., wide estuaries, bays, capes, islands) and artificial (e.g., seawalls, breakwaters), could significantly modify the spreading of river plumes and, therefore, distort the deflection angle inherent for the

related latitude [29]. Finally, the spreading direction of a river plume could be modified and distorted in case of strong ambient coastal or tidal circulation [30–32]. As a result, an analysis of the spreading of specific river plumes under wind forcing requires the examination of the limitations listed above before applying the result of the dependence of deflection angle on latitude. In addition, the obtained results about river plumes are not directly applicable to other substances in the sea surface layer, including oil plumes [33–36], suspended and floating pollutants [37,38], thermal plumes [39,40], etc., due to significant differences in forces, which govern their spreading dynamics.

Future research needs in this field are related to a more detailed understanding of wind-driver circulation within river plumes. According to previous studies and the current work, the general horizontal circulation in small- and medium-sized plumes forms surface flow from the estuarine zone towards the far-field part of a plume, which direction is determined by wind forcing conditions. However, the vertical structure of this flow, spatial velocity variability of this flow across the plume, existence of reverse flows, etc., remain mostly unknown. The study of these processes requires synchronous application of specialized in situ measurements, aerial observations using quadcopters, and usage of drifters or unmanned autonomous marine vehicles equipped with temperature and salinity sensors.

Author Contributions: Conceptualization, A.O.; methodology, A.O. and I.A.; satellite data processing, I.A. and V.R.; investigation, A.O. and I.A.; writing, A.O., I.A. and V.R. All authors have read and agreed to the published version of the manuscript.

Funding: This research was funded by the Ministry of Science and Higher Education of the Russian Federation, theme FMWE-2021-0001 (collecting and processing of satellite data) and the Russian Scientific Foundation, project 23-17-00087 (study of river plumes).

Data Availability Statement: The Sentinel-2 satellite data are available at the Copernicus Open Access Hub (https://scihub.copernicus.eu/, accessed on 15 May 2023). The Landsat 8 Surface Reflectance Level-2 products are available at the United States Geological Survey website (http://earthexplorer.usgs.gov, accessed on 15 May 2023). The ERA5 reanalysis data are available at the European Centre for Medium-Range Weather Forecasts website (https://www.ecmwf.int/en/forecasts/datasets/archive-datasets/reanalysisdatasets/era5, accessed on 15 May 2023). The analyzed data are available at https://doi.org/10.5281/zenodo.8003006 (accessed on 4 June 2023).

Conflicts of Interest: The authors declare no conflict of interest.

References

1. Simpson, J.H.; Sharples, J.; Rippeth, T.P. A prescriptive model of stratification induced by freshwater runoff. *Estuar. Coast. Shelf Sci.* **1991**, *33*, 23–35. [CrossRef]
2. Kang, Y.; Pan, D.; Bai, Y.; He, X.; Chen, X.; Chen, C.T.A.; Wang, D. Areas of the global major river plumes. *Acta Oceanol. Sin.* **2013**, *32*, 79–88. [CrossRef]
3. Tang, D.; Kester, D.R.; Ni, I.H.; Qi, Y.; Kawamura, H. In situ and satellite observations of a harmful algal bloom and water condition at the Pearl River estuary in late autumn 1998. *Harmful Algae* **2003**, *2*, 89–99. [CrossRef]
4. Boyer, E.W.; Howarth, R.W.; Galloway, J.N.; Dentener, F.J.; Green, P.A.; Vörösmarty, C.J. Riverine nitrogen export from the continents to the coasts. *Glob. Biogeochem. Cycles* **2006**, *20*, GB1S9. [CrossRef]
5. Milliman, J.D.; Farnsworth, K.L. *River Discharge to the Coastal Ocean: A Global Synthesis*; Cambridge University Press: Cambridge, UK, 2013; 393p.
6. Osadchiev, A.A. Spreading of the Amur river plume in the Amur Liman, the Sakhalin Gulf, and the Strait of Tartary. *Oceanology* **2017**, *57*, 376–382. [CrossRef]
7. Hetland, R.D. Relating river plume structure to vertical mixing. *J. Phys. Oceanogr.* **2005**, *35*, 1667–1688. [CrossRef]
8. Horner-Devine, A.R.; Hetland, R.D.; MacDonald, D.G. Mixing and transport in coastal river plumes. *Ann. Rev. Mar. Sci.* **2015**, *47*, 569–594. [CrossRef]
9. Spicer, P.; Cole, K.L.; Huguenard, K.; MacDonald, D.G.; Whitney, M.M. The effect of bottom-generated tidal mixing on tidally pulsed river plumes. *J. Phys. Oceanogr.* **2021**, *51*, 2223–2241. [CrossRef]

10. Osadchiev, A.; Gordey, A.; Barymova, A.; Sedakov, R.; Rogozhin, V.; Zhiba, R.; Dbar, R. Lateral border of a small river plume: Salinity structure, instabilities and mass transport. *Remote Sens.* **2022**, *14*, 3818. [CrossRef]
11. Zu, T.; Wang, D.; Gan, J.; Guan, W. On the role of wind and tide in generating variability of Pearl River plume during summer in a coupled wide estuary and shelf system. *J. Mar. Sys.* **2014**, *136*, 65–79. [CrossRef]
12. Otero, P.; Ruiz-Villarreal, M.; Peliz, A. Variability of river plumes off Northwest Iberia in response to wind events. *J. Mar. Syst.* **2008**, *72*, 238–255. [CrossRef]
13. Osadchiev, A.A.; Barymova, A.A.; Sedakov, R.O.; Zhiba, R.Y.; Dbar, R.Y. Spatial structure, short-temporal variability, and dynamical features of small river plumes as observed by aerial drones: Case study of the Kodor and Bzyp river plumes. *Remote Sens.* **2020**, *12*, 3079. [CrossRef]
14. Osadchiev, A.A.; Sedakov, R.O.; Barymova, A.A. Response of a small river plume on wind forcing. *Front. Mar. Sci.* **2021**, *8*, 1910. [CrossRef]
15. Basdurak, N.B.; Largier, J.L. Wind effects on small-scale river and creek plumes. *J. Geophys. Res. Ocean.* **2022**, *127*, e2021JC018381. [CrossRef]
16. O'Donnell, J. The formation and fate of a river plume: A numerical model. *J. Phys. Oceanogr.* **1990**, *20*, 551–569. [CrossRef]
17. Ekman, V.W. On the influence of the earth's rotation on ocean currents. *Ark. Mat. Astron. Fys.* **1905**, *2*, 1874–1954.
18. Yankovsky, A.E.; Chapman, D.C. A simple theory for the fate of buoyant coastal discharges. *J. Phys. Oceanogr.* **1997**, *27*, 1386–1401. [CrossRef]
19. Osadchiev, A.A.; Zavialov, P.O. Structure and dynamics of plumes generated by small rivers. In *Estuaries and Coastal Zones—Dynamics and Response to Environmental Changes*; Pan, J., Devlin, A., Eds.; IntechOpen: London, UK, 2020. [CrossRef]
20. Zhurbas, N.V. The wind-induced drift velocity of the freshwater layer on the sea's surface. *Oceanology* **2013**, *53*, 136–144. [CrossRef]
21. Osadchiev, A.; Sedakov, R. Spreading dynamics of small river plumes off the northeastern coast of the Black Sea observed by Landsat 8 and Sentinel-2. *Remote Sens. Environ.* **2019**, *221*, 522–533. [CrossRef]
22. Hersbach, H.; Bell, B.; Berrisford, P.; Hirahara, S.; Horányi, A.; Muñoz-Sabater, J.; Nicolas, J.; Peubey, C.; Radu, R.; Schepers, D.; et al. The ERA5 global reanalysis. *Q. J. R. Meteorol. Soc.* **2020**, *146*, 1999–2049. [CrossRef]
23. Madsen, O.S. A realistic model of the wind-induced Ekman boundary layer. *J. Phys. Oceanogr.* **1977**, *7*, 248–255. [CrossRef]
24. Kirwan, A.D., Jr.; McNally, G.; Pazan, S.; Wert, R. Analysis of surface current response to wind. *J. Phys. Oceanogr.* **1979**, *9*, 401–412. [CrossRef]
25. Milliman, J.D.; Syvitski, J.P.M. Geomorphic/tectonic control of sediment discharge to the ocean: The importance of small mountainous rivers. *J. Geol.* **1992**, *100*, 525–544. [CrossRef]
26. Wheatcroft, R.A.; Goni, M.A.; Hatten, J.A.; Pasternack, G.B.; Warrick, J.A. The role of effective discharge in the ocean delivery of particulate organic carbon by small, mountainous river systems. *Limnol. Oceanogr.* **2010**, *55*, 161–171. [CrossRef]
27. Korotkina, O.A.; Zavialov, P.O.; Osadchiev, A.A. Submesoscale variability of the current and wind fields in the coastal region of Sochi. *Oceanology* **2011**, *51*, 745–754. [CrossRef]
28. Korotkina, O.A.; Zavialov, P.O.; Osadchiev, A.A. Synoptic variability of currents in the coastal waters of Sochi. *Oceanology* **2014**, *54*, 545–556. [CrossRef]
29. Zavialov, I.B.; Osadchiev, A.A.; Sedakov, R.O.; Barnier, B.; Molines, J.-M.; Belokopytov, V.N. Water exchange between the Sea of Azov and the Black Sea through the Kerch Strait. *Ocean Sci.* **2020**, *16*, 15–30. [CrossRef]
30. Nikiema, O.; Devenon, J.-L.; Baklouti, M. Numerical modeling of the Amazon River plume. *Cont. Shelf Res.* **2007**, *27*, 873–899. [CrossRef]
31. Nash, J.D.; Kilcher, L.F.; Moum, J.N. Structure and composition of a strongly stratified, tidally pulsed river plume. *J. Geophys. Res. Ocean* **2009**, *114*, C00B12. [CrossRef]
32. Osadchiev, A.A.; Medvedev, I.P.; Shchuka, S.A.; Kulikov, M.E.; Spivak, E.A.; Pisareva, M.A.; Semiletov, I.P. Influence of estuarine tidal mixing on structure and spatial scales of large river plumes. *Ocean Sci.* **2020**, *16*, 781–798. [CrossRef]
33. Ivanov, A.Y. The oil spill from a shipwreck in Kerch Strait: Radar monitoring and numerical modelling. *Int. J. Remote Sens.* **2010**, *31*, 4853–4868. [CrossRef]
34. Nemirovskaya, I.A.; Zavialov, P.O.; Khramtsova, A.V. Hydrocarbon pollution in the waters and sediments of the Kerch Strait. *Mar. Pol. Bull.* **2022**, *180*, 113760. [CrossRef]
35. Korotenko, K.A.; Mamedov, R.M.; Kontar, A.E.; Korotenko, L.A. Particle tracking method in the approach for prediction of oil slick transport in the sea: Modelling oil pollution resulting from river input. *J. Mar. Syst.* **2004**, *48*, 159–170. [CrossRef]
36. Korotenko, K.A. Effects of mesoscale eddies on behavior of an oil spill resulting from an accidental deepwater blowout in the Black Sea: An assessment of the environmental impacts. *PeerJ* **2018**, *6*, e5448. [CrossRef]
37. Korshenko, E.A.; Zhurbas, V.M.; Osadchiev, A.A.; Belyakova, P.A. Fate of river-borne floating litter during the flooding event in the northeastern part of the Black Sea in October 2018. *Mar. Pol. Bull.* **2020**, *160*, 111678. [CrossRef]
38. Pogojeva, M.; Zhdanov, I.; Berezina, A.; Lapenkov, A.; Kosmach, D.; Osadchiev, A.; Hanke, G.; Semiletov, I.; Yakushev, E. Distribution of floating marine macro-litter in relation to oceanographic characteristics in the Russian Arctic Seas. *Mar. Pol. Bull.* **2021**, *166*, 112201. [CrossRef] [PubMed]

39. Tang, D.; Kester, D.R.; Wang, Z.; Lian, J.; Kawamura, H. AVHRR satellite remote sensing and shipboard measurements of the thermal plume from the Daya Bay, nuclear power station, China. *Remote Sens. Environ.* **2003**, *84*, 506–515. [CrossRef]
40. Duran-Colmenares, A.; Barrios-Pina, H.; Ramirez-Leon, H. Numerical modeling of water thermal plumes emitted by thermal power plants. *Water* **2016**, *8*, 482. [CrossRef]